Pergamon

Chaos, Solitons & Fractals Vol. 4, No. 11, pp. 2077–2092, 1994

0960–0779/94$7.00 + .00

0960–0779(95)E0127–B

Topology-preserving Mappings in a Self-imaging Photorefractively Pumped Ring Resonator

M. SAFFMAN,* D. MONTGOMERY, A. A. ZOZULYA and D. Z. ANDERSON

Department of Physics and Joint Institute for Laboratory Astrophysics, University of Colorado, Boulder, CO 80309-0440, USA

(*Received* 21 *January* 1994)

Abstract—We present a photorefractively pumped ring resonator for the formation of self-organized, topology-preserving mappings. The self-imaging ring resonator with saturable gain and loss supports localized cavity modes at arbitrary transverse locations. When the resonator is pumped by two uncorrelated signals, two spatially well separated modes form. Each mode is correlated temporally with one of the input signals. When the resonator is pumped by partially correlated inputs, modes with a partial spatial overlap form. The spatial distribution of the modes preserves the spatial topology of the input signals. An experimental demonstration and numerical simulations are presented.

1. INTRODUCTION

Optical resonators have been used to demonstrate information-processing tasks inspired by neural network models of computation. Associative memories are the most frequently cited examples. They have been implemented with photorefractive ring resonators [1, 2], phaseconjugating photorefractive resonators [3, 4], and lasers with active media [5]. An associative memory embodies two distinct phases of operation. A learning phase where information is stored in the memory, and a processing, or recall phase, where new data is compared with the stored information. In all the cited demonstrations [1–5] the learning phase was performed manually. That is to say, some preselected images were stored in the resonator, or in external fixed holograms, prior to the recall phase.

This contribution is a continuation of recent work with self-organizing feature extractors [6, 7] that incorporate an unsupervised learning phase. By using a more sophisticated optical architecture, we are able to generalize the feature extractor, which is intended for spatially uncorrelated inputs, to the case of spatially correlated input signals. The photorefractive resonator performs a continuous mapping of input signals onto localized resonator modes. The spatial correlations of the resonator modes preserve the topology, as defined by the correlations of the input signals.

A self-organizing resonator architecture learns to recognize features in complex, information bearing beams. Due to the dynamics of competition between the transverse modes of the resonator, different input features are mapped onto different groups of resonator modes. In the recall phase, where new data is presented to the resonator, groups of modes turn on, depending on the degree of similarity between the training set used in the learning phase, and the new inputs. The recall phase of the feature extractor is fundamentally different from the recall phase of an associative memory. In the associative memory the signal that is injected in the recall phase biases the nonlinear mode competition to favor the

*Present address: RISØ National Laboratory, Optics and Fluid Dynamics Department, P.O. Box 49, DK-4000 Roskilde, Denmark.

stored resonator eigenmode that most closely matches the input [1]. Thus, a mode containing complete information is excited associatively when the resonator is presented with partial information. All other resonator modes are suppressed. In the feature extractor, the recall phase is purely linear. When partial information is presented, all linearly dependent resonator modes are excited, not only the mode corresponding to the training pattern that bears the greatest resemblance to the new input.

The recent demonstrations of self-organizing feature extractors [6, 7] were based on resonators with a fixed mode structure. For example, a composite resonator, composed of two rings of multimode fiber, was used to separate two spatially scrambled signals. Each input signal was mapped to one of the fiber rings. In the work described here, we demonstrate a self-organized learning system that is more sophisticated than the simple feature extractor. We use a self-imaging resonator where the transverse mode structure is strongly influenced by the nonlinear gain and loss, and only weakly affected by the linear boundary conditions. By placing saturable photorefractive gain and loss in spatially distinct resonator planes the continuum of transverse modes collapses to a localized, singlemode-like oscillation, at an arbitrary transverse location in the resonator [8]. This architecture allows a more general class of mappings to be implemented than is possible in resonators with a fixed mode structure. Besides feature extraction, we demonstrate a continuous topology-preserving mapping of partially correlated inputs, onto spatially overlapping transverse modes of the resonator.

Topology-preserving feature maps [9, 10] that form due to a process of self-organization, are of interest, both in the context of understanding the development of sensory functionality in biological systems [11], and for solving difficult computational tasks such as the 'traveling salesman problem' [10]. The function of the topology-preserving map is to order a large set of data, such that similar items in the input space are represented by similar locations in the output space. In many cases the output space may be of lower dimensionality than the input space. As introduced by Kohenen [12], the topology-preserving map is an algorithm that is straightforward to implement on a digital computer, but difficult to envision in a physical system. One goal of this contribution is to demonstrate a physical system, as opposed to a computer program, that has the same functionality as Kohenen's algorithm.

Kohenen's algorithm is based on two essential components. The first is an adaptable interconnection network that maps data from an input layer to an output layer. The second is a set of lateral connections, within the output layer, that implement a modified version of the so-called 'winner takes all' function. When data are presented to the input layer of the network, some location in the output layer will have the strongest response. Kohenen's algorithm prescribes that the connections between the input and the point of strongest response should be strengthened. However, in contrast to a pure 'winner takes all' algorithm, the connections to the local region surrounding the point of strongest response are also strengthened. It is this additional updating of the connections to a spatially localized region that give the algorithm its topological properties.

The essential elements of Kohenen's algorithm correspond, using an admittedly over-simplified description, to different parts of the self-imaging resonator with gain and loss. The adjustable interconnection network is simply the index grating in the volume of the photorefractive gain crystal. This grating adaptively connects spatially complex input signals with transverse resonator modes. The photorefractive loss crystal causes the complicated transverse mode structure to collapse to a localized, singlemode-like oscillation. This corresponds to the modified 'winner takes all' behavior [13].* Feedback provided by the

*Winner takes all behavior in a resonator with discrete modes was demonstrated in ref. [13].

optical cavity serves to connect these two elements. The result is a dynamical evolution that implements the functionality of Kohenen's algorithm.

Experimental demonstrations of feature extraction and topology preserving mappings are described in Section 2. The demonstrations employ speckle fields that are generated by propagation in a multimode fiber. The speckle fields are spatially uncorrelated in the case of the feature extractor, while they are prepared to have a finite correlation in the demonstration of a topology-preserving mapping. When the input signals are uncorrelated spatially well separated modes form in the resonator. Each of the modes is temporally correlated with one of the input signals. When the input signals are spatially correlated spatially overlapping modes form in the resonator. The spatial correlation of the resonator modes is observed to vary continuously, as a function of the input correlation. In Section 3 we develop a two-dimensional model for the resonator dynamics based on the equations of photorefractive nonlinear optics. The equations are solved numerically in Section 4. The numerical results agree qualitatively with the experimentally observed behavior. Furthermore, the numerical results show that the mapping tends to be contracted: the correlation inside the resonator is always greater than the input correlation. While the numerical calculations serve to corroborate the experimental results, they offer little insight into the reason for the observed behavior. Semianalytical arguments based on a simplified plane-wave model are given in Section 5. The plane-wave model shows that the input signals do not map onto the same resonator mode because the oscillating intensity is maximized when the input signals map onto different resonator modes. The main results are summarized in Section 6.

2. EXPERIMENTAL RESULTS

In this section we present experimental observations of feature-extraction and topology-preserving mappings in a self-imaging photorefractive resonator. A detailed description of the resonator, and the formation of localized transverse modes, has been given in [8]. For completeness we include a short description of the resonator geometry below.

The transverse-mode profile in a high Fresnel number self-imaging optical cavity is not well defined. The observed transverse structure is a continuously changing superposition of many metastable transverse modes. Several groups have recently demonstrated self-induced conversion of a complicated transverse structure into a localized mode with a well-defined profile [8, 14, 15]. The basic approach in all of these demonstrations is similar: combine saturable gain in one plane of the resonator with saturable loss in a spatially distinct plane. The spatial mode naturally adjusts itself until the net gain is maximized. The result is a transverse mode that is highly localized in the plane of the loss medium, since this gives the largest possible loss saturation for given oscillating power. When the optical cavity is self-imaging [8, 15], such that there are no preferred transverse modes, the localized mode can form at an arbitrary transverse location.

The optical geometry is shown in Fig. 1. Planes labeled $\mathcal{G}$ are imaged onto each other, and planes labeled $\mathcal{L}$ are imaged onto each other, while $\mathcal{G}$ and $\mathcal{L}$ are spatially conjugate planes. The field profiles in the planes of the gain and loss media are therefore Fourier transforms of each other. The resonator Fresnel number is given by $\mathcal{F} = r_{\max}^2/\pi\omega_c^2$, where $r_{\max}$ is the limiting iris radius, and $\omega_c = \sqrt{(\lambda f_1/\pi)}$ is the confocal mode radius of the equivalent linear resonator. All of the data presented here were taken with $r_{\max} = 3.5$ mm, giving $\mathcal{F} \sim 240$. Setting the pump beam radius to $\omega_p = \omega_c$ gives a localized mode in the loss plane with radius $(f_3/f_2)\omega_p$. The demagnification provided by lenses f_2 and f_3 increases the intensity in the loss medium. Since the photorefractive time constant is inversely proportional to the intensity, the increase in intensity speeds up the response of the loss medium.

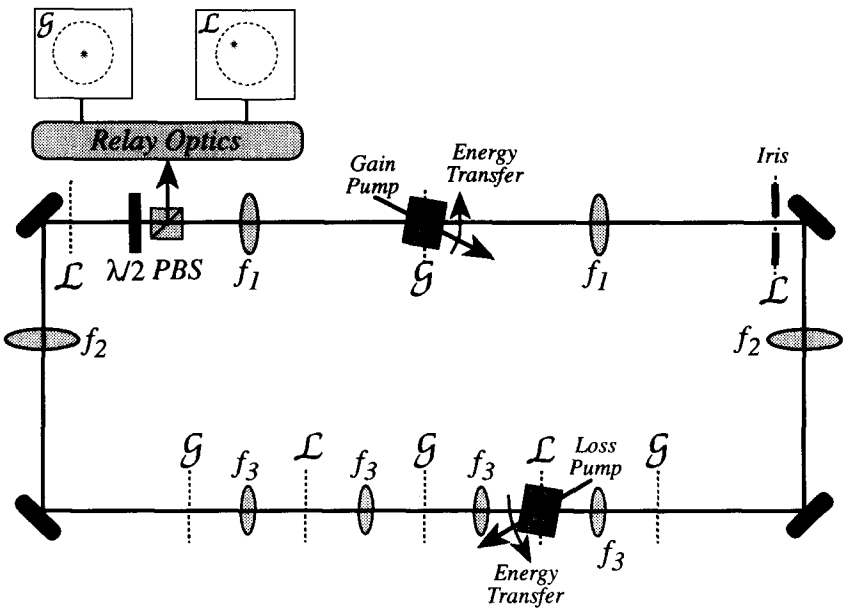

Fig. 1. Self-imaging ring resonator with photorefractive ($BaTiO_3$) gain and loss. The gain and loss pumps are from a cw Argon-ion laser, $\lambda = 514$ nm, all beams are polarized in the plane of the figure, the gain pump is a speckle beam with radius $r_p \sim w_c \simeq 260\ \mu$m, and the loss pump is an expanded copy of the speckle beam with a radius of ~ 5.5 mm. The coupling and time constants of the gain and loss crystals are $G = 4.9$, $\tau_{0_g} = 4.2\ \text{sec W cm}^{-2}$, and $L = 2.1$, $\tau_{0_l} = 0.061\ \text{sec W cm}^{-2}$, where the small signal gain and loss are given by $\exp(G)$ and $\exp(-L)$. The lenses are $f_1 = 100$ mm, $f_2 = 150$ mm, $f_3 = 30$ mm, all lenses are confocally spaced, and the passive cavity reflectivity is $R = \exp(-C)$, $C = 3.4$. The data presented here were obtained with a limiting iris radius $r_{\max} = 3.5$ mm, giving a Fresnel number $\mathcal{F} \sim 240$.

This is necessary in order to ensure that the resonator prefers a localized mode structure [8].

The dynamics of the localized modes depend strongly on the cavity alignment. For small cavity misalignment, such that the transverse phase mismatch across the limiting iris is $\sim \leq \pi$, the transverse location of the localized mode becomes unstable [8]. The cavity misalignment causes a linear feeding of energy from the oscillating mode to neighboring locations. This results in a continuous drifting of the spot in the transverse plane of the resonator. Simulation of the drift instability [16] shows that it persists for arbitrarily small cavity misalignment. We wish to use the resonator modes as static representations of the images pumping the resonator. It is therefore necessary to eliminate the drift motion. The stabilization method used here is simply to misalign the optical cavity such that the transverse phase mismatch is several π. In this case the oscillating pattern, with no loss pumping, is a set of fringes that represent the cavity equiphase contours. When the loss pump is turned on localized modes still form, but they are restricted to locations on the bright fringes. The dark fringes act as barriers to the drift motion. The maximum number of fringes consistent with the formation of localized modes is [8] $N_{\max} \leq \sqrt{(\pi\mathcal{F})/2}$, which in the geometry of Fig. 1 gives $N_{\max} \sim 14$. The experiments reported here were performed with $N \sim 7$. The disadvantage of this approach to mode stabilization is that the modes can no longer form at arbitrary transverse locations. However, modes can still form at arbitrary locations along a single fringe. Thus, the resonator described here is suitable for implementing mappings from a two-dimensional input space to a one-dimensional transverse mode distribution.

The pump beam to the photorefractive gain crystal need not have a smooth Gaussian

transverse profile. Since the photorefractive gain results from diffraction in a volume hologram, arbitrary spatial-pump profiles may be transformed into arbitrary resonator-mode profiles. When a Gaussian beam is propagated through a length of multimode fiber it emerges as a speckle pattern. Pumping the resonator with a speckle pattern also leads to a mode with a smooth, localized envelope. When the resonator is pumped with two spatially distinct speckle patterns, each one leads to a localized mode. When the speckle patterns are spatially and temporally orthogonal, the resulting resonator modes are also spatially and temporally orthogonal. Thus the resonator acts as a feature extractor.

The input signals for the feature extraction experiment are prepared using the arrangement of Fig. 2(a). The acousto-optic modulators are turned on at alternate times, so the inputs are never present simultaneously. Both modulators are driven from the same 80 MHz oscillator so that the first-order diffracted beams that are coupled into the fiber have the same carrier frequency. The output of the fiber is imaged onto the gain crystal of the resonator in Fig. 1 with $\times 2.5$ magnification. This gives a pump beam spot radius of $\omega_p = 125\ \mu$. The fiber output is imaged onto the loss crystal with $\times 80$ magnification to cover uniformly the available aperture. The resonator mode with the loss pump blocked is shown in the top row of Fig. 3. Each input leads to a multimode oscillation. The two oscillation patterns have a high degree of similarity, but are not identical. The loss pump beam is then turned on. The multimode oscillations collapse to two nearly singlemode oscillations, shown in the bottom row of Fig. 3. The intensity overlap and crosstalk between the modes are very low.

The topology-preserving mapping is demonstrated using partially correlated input signals. The correlated inputs are derived by continuous angular scanning of the input beam using a galvanometer mirror, as shown in Fig. 2(b). The limits of the galvanometer scan were set to correspond to approximately zero intensity overlap, as shown in Fig. 4(a). The scanning was driven by a sawtooth waveform such that all input positions were sampled equally. The

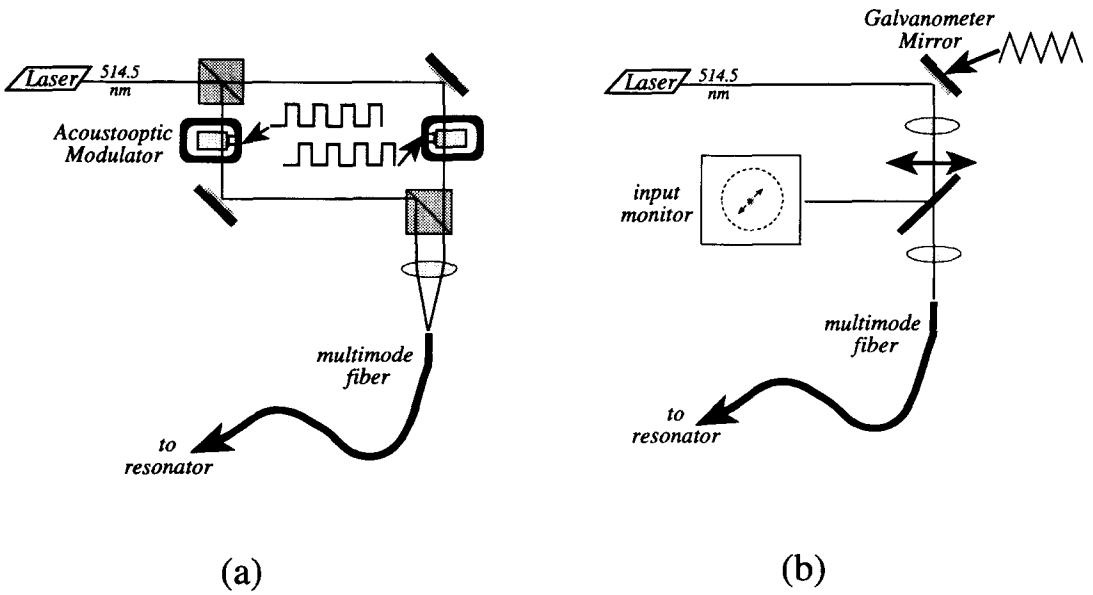

Fig. 2. Optical geometry for generating input signals. In (a) spatially orthogonal speckle patterns are generated in alternate time slots. In (b) a continuous distribution of signals is generated by scanning the beam coupled into the fiber. The fiber is multimode 100/140 μ diameter and 5 m long.

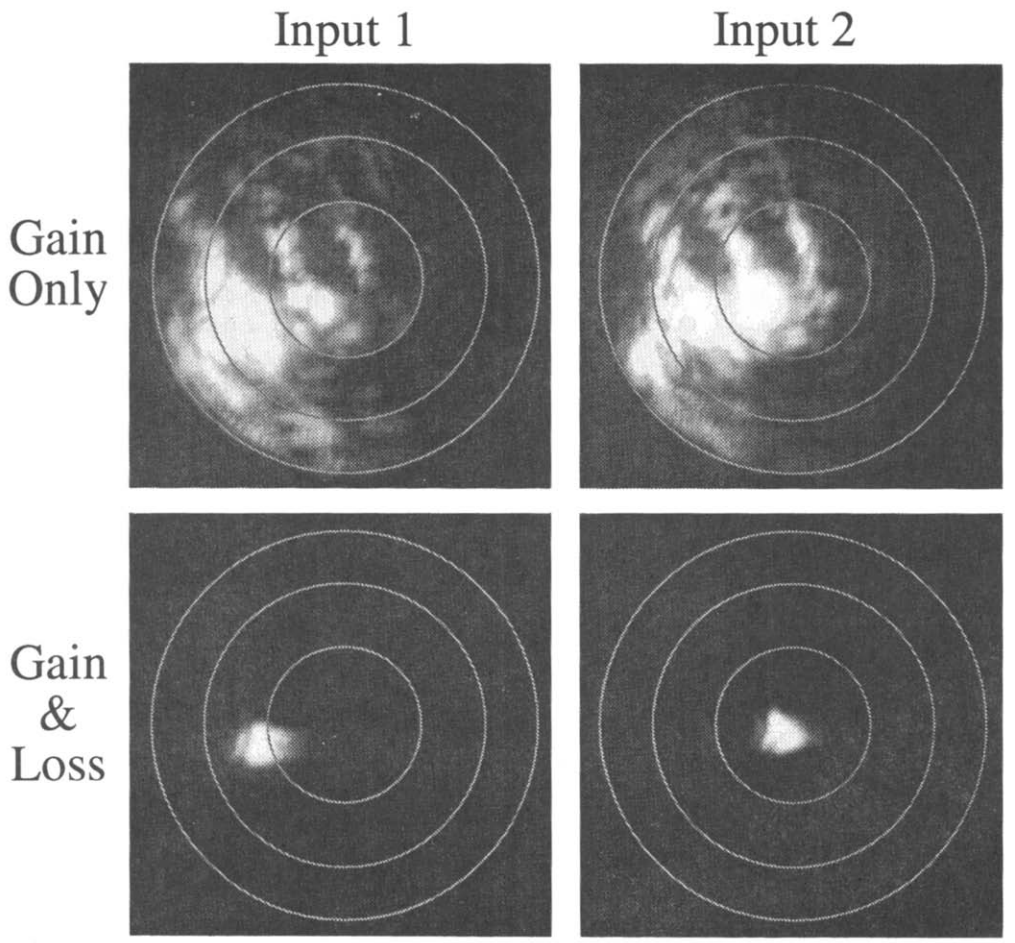

Fig. 3. Experimental observation of feature extraction. The two columns show the resonator mode with inputs 1 or 2 turned on. The top row shows the resonator mode with gain only. The bottom row shows the localized modes with gain and loss. The concentric rings were superimposed on the picture as an aid to the viewer. The region within the outermost ring corresponds to a resonator Fresnel number of 240.

resonator modes corresponding to the input beam position are shown in Fig. 4(b). The modes corresponding to the limits of the input scan have a low spatial correlation. The significant aspect of the data shown in Fig. 4 is that the spatial location of the resonator mode varies continuously. The similarity between resonator modes at different times reflects the similarity between input patterns at different times. The measure of similarity is the inner product, $h \sim \int \mathrm{d}x s_1(x) s_2^*(x)$, of two input signals. Neighboring input patterns are mapped onto neighboring resonator modes, while well-separated input patterns are mapped onto well-separated resonator modes. This is not an obvious result since the resonator only sees the speckle patterns coming out of the multimode fiber. The functionality of the resonator modes is equivalent to that of Kohenen's algorithm [9] for a self-organizing topology-preserving mapping.

3. MODEL EQUATIONS

The dynamical behavior of the self-imaging ring resonator with photorefractive gain and loss is described by a set of equations for the coupled field and material dynamics in each

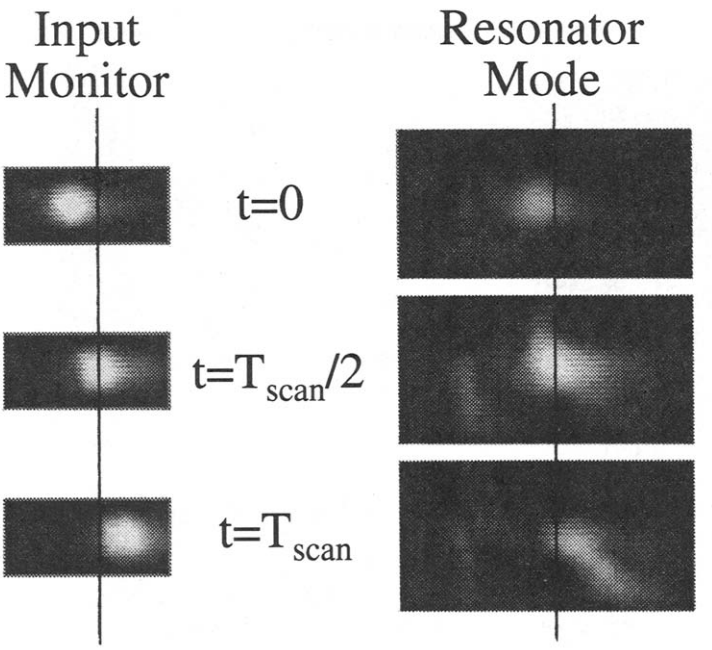

Fig. 4. Experimental observation of a topology preserving mapping. The position of the input beam as seen at the input monitor in Fig. 2(b) is shown in the column on the left. The corresponding resonator mode is shown in the column on the right. The vertical lines are drawn through the centroids of the intensity profiles halfway through the spatial scan. The displayed region of the transverse resonator aperture corresponds to a Fresnel number of ~ 20.

photorefractive crystal, together with boundary conditions that connect the two crystals. The photorefractive interaction in the gain medium, shown in detail in Fig. 5, is described in the paraxial limit in one transverse dimension by the set of equations

$$\left(\frac{\partial}{\partial z} + \theta_{r,g}\frac{\partial}{\partial x} - \frac{i}{2k}\frac{\partial^2}{\partial x^2}\right) r_{\omega,g}(x, z, t) = g_g(x, z, t) s_{\omega,g}(x, z, t), \tag{1a}$$

$$\left(\frac{\partial}{\partial z} - \theta_{s,g}\frac{\partial}{\partial x} - \frac{i}{2k}\frac{\partial^2}{\partial x^2}\right) s_{\omega,g}(x, z, t) = -g_g^*(x, z, t) r_{\omega,g}(x, z, t), \tag{1b}$$

$$\left(\tau_g\frac{\partial}{\partial t} + 1\right) g_g(x, z, t) = \frac{\Gamma_g}{2I_g}\sum_{\omega} r_{\omega,g}(x, z, t) s^*_{\omega,g}(x, z, t). \tag{1c}$$

Here the subscript g labels the gain medium. s and r are the slowly varying amplitudes of the input signal (pump beam) and resonator fields, g is the induced photorefractive grating, $\tau_g(I_g) = \tau_{0_g}/I_g$ is the intensity-dependent photorefractive time constant, $I_g = \sum_\omega |r_{\omega,g}|^2 + |s_{\omega,g}|^2$ is the total intensity, and $k = 2\pi n/\lambda$ is the wavevector. The form of equations (1) implicitly assumes that the angle between the beams $(\theta_r + \theta_s)$ is much larger than the angular divergence of each beam individually. Equations (1) are correct to order $\theta^2_{(r,s)}$, where $\theta_{(r,s)}$ are the mean angles of propagation of the signal and resonator beams with respect to the z-axis. Thus noncollinearity of the signal and resonator fields inside the photorefractive medium is explicitly accounted for. Crossing of the signal and resonator fields enables correlations between the input signals to be computed effectively by the photorefractive interaction. Numerical calculations that do not include the effect of beam crossing do not result in topology-preserving mappings. The coupling constant Γ will be assumed real, which corresponds to a medium with a purely diffusional response, and

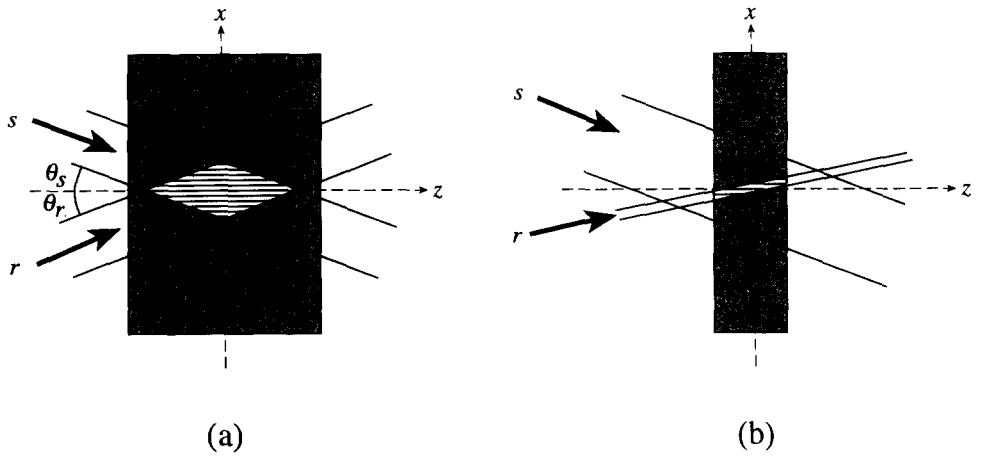

Fig. 5. Geometry of the photorefractive media. The gain interaction is shown in (a) and the loss interaction in (b).

linear absorption has been neglected. It should be emphasized that equations (1) allow for arbitrary longitudinal variation of both the signal and resonator fields inside the photorefractive medium. This is necessary, since the experimental results were obtained in a resonator with cavity reflectivity of only a few percent. A mean field formulation of the problem, such as that used in ref. [17], would not be appropriate here.

In the experimental demonstrations described in Section 2, different signals were presented at different times. Alternatively, the signals could be multiplexed on different optical carrier frequencies [6]. As long as the separation between carrier frequencies satisfies $\Delta\omega \gg 1/\tau$, the two approaches are equivalent. As used in equations (1), ω is a generic label for temporally orthogonal signals [18] that do not interfere to write a photorefractive grating.

The interaction in the loss medium is shown in Fig. 5(b). Since the loss pump has been expanded to cover the photorefractive medium uniformly, most of the beam-crossing region lies outside the medium. The two-dimensional nature of the interaction may therefore be neglected leading to the simplified set of equations

$$\frac{\partial}{\partial z} r_{\omega,l}(x, z, t) = g_l(x, z, t) s_{\omega,l}(x, z, t), \tag{2a}$$

$$\frac{\partial}{\partial z} s_{\omega,l}(x, z, t) = -g_l^*(x, z, t) r_{\omega,l}(x, z, t), \tag{2b}$$

$$\left(\tau_l \frac{\partial}{\partial t} + 1\right) g_l(x, z, t) = \frac{\Gamma}{2I_l} \sum_{\omega} r_{\omega,l}(x, z, t) s_{\omega,l}^*(x, z, t). \tag{2c}$$

Here subscript l labels the loss medium. Diffraction has also been neglected since the Rayleigh lengths of localized modes with characteristic diameters of ~ 0.1 mm is much larger than the crystal depth of ~ 5 mm.

The equations of motion in the gain and loss media are supplemented by the boundary conditions

$$s_{\omega,g}(x, z = 0, t) = s_{\omega,g}^{(0)}(x), \tag{3a}$$

$$s_{\omega,l}(x, z = 0, t) = s_{\omega,l}^{(0)}(x), \tag{3b}$$

$$r_{\omega,g}(x, z = 0, t) = \epsilon(x, t) s_{\omega,g}^{(0)}(x) + e^{-C/2} \mathcal{F}^{-1}[r_{\omega,l}(x, z = l_l, t)], \tag{3c}$$

$$r_{\omega,l}(x, z = 0, t) = \mathcal{F}[r_{\omega,g}(x, z = l_g, t)], \tag{3d}$$

$$g_g^*(x, z, 0) = g_l^*(x, z, 0) = 0. \tag{3e}$$

$\epsilon(x, t)$ is a small coefficient that models seeding of the oscillation by random scattering at the crystal surface, $\mathcal{F}$ is the spatial Fourier transform operator, and the cavity reflectivity given by $R = e^{-C}$ is lumped to lie between the loss and gain media. The finite cavity-propagation time is neglected, since for the experimental conditions of Section 2, it is much smaller than the photorefractive relaxation time τ.

Equations (1) and (2) describe the response of the resonator to a set of temporally orthogonal signals. This is an appropriate description of the feature extractor. In the case of the continuous distribution of partially correlated inputs used to demonstrate the topology-preserving mapping, some caution is required. Although the equations of motion may be formulated to describe this situation correctly, their numerical evaluation becomes expensive. We will therefore use equations (1) and (2) to describe topology-preserving mappings, assuming a discrete set of spatially correlated, but temporally orthogonal input signals. Kohenen's algorithm has been applied to discrete, as well as continuous input distributions. The results are in both cases similar [10, section 6.2].

4. NUMERICAL RESULTS

We have numerically simulated the response of the photorefractive resonator as described by equations (1)–(3). The main result of the calculations is a prediction of how the degree of spatial correlation of the resonator fields depends on the correlation of the input signals, and the resonator parameters. In order to reduce the computational burden, the calculations were performed using smooth Gaussian input beams, instead of speckled beams. Calculations with speckled beams would change the numerical details of the results reported below, but not the general behavior. In the absence of losses, propagation in a multimode optical fiber is described by a unitary transformation of the field, that preserves inner products. This has been verified experimentally [19]. Thus, for the numerical results shown in Figs 6–9, the input signals were

$$s_{1,g}^{(0)}(x) = A_{1,g} \exp(i\kappa_1 x) \exp(-x^2/\omega^2), \tag{4a}$$

$$s_{2,g}^{(0)}(x) = A_{2,g} \exp(i\kappa_2 x) \exp(-x^2/\omega^2), \tag{4b}$$

$$s_{1,l}^{(0)}(x) = A_{1,l} \exp(i\kappa_1 x), \tag{4c}$$

$$s_{2,l}^{(0)}(x) = A_{2,l} \exp(i\kappa_2 x), \tag{4d}$$

where κ, which is proportional to the angle of propagation, determines the degree of overlap of the input beams, and A is the field amplitude. The input beams to the loss crystal were assumed to have a constant transverse intensity, as was the case in the experiments described in Section 2. The spatial correlation of the input beams is defined by

$$h_{ij}^{(0)} = \frac{|\int dx s_{i,g}^{(0)} s_{j,g}^{(0)*}|^2}{\int dx |s_{i,g}^{(0)}|^2 \int dx |s_{j,g}^{(0)}|^2}, \tag{5}$$

with an analogous definition for the correlation $h_{ij}^{(g,l)}$ of the resonator fields at the output face of the gain and loss crystals.

Equations (1) were solved on a grid of 350 (along x) × 250 (along z) points using a finite difference Crank–Nicholson type scheme [20] for the spatial integration, together with a second-order accurate method for the temporal evolution. The resonator axis was chosen

to lie along z so $\theta_{s,g} = 0$. The other parameters were $\theta_{r,g} = 7°$, $\lambda = 0.514\ \mu$m, $n = 2.4$, the crystal width along x was 0.6 mm, the crystal thickness along z was $l_g = 2.0$ mm, and $\omega = 0.06$ mm. Since we are interested in the steady-state behavior, we set $\tau_l = 0$ in equation (2) (i.e. instantaneous loss). The spatial integration of the fields in the loss medium was performed using a Runge–Kutta method, and the other parameters were the same as for the gain medium. The input signals were of equal intensity ($A_{1,(g,l)} = A_{2(g,l)}$), and the loss pump intensity was 0.04 times the peak intensity of the gain pump. The oscillation was seeded using a low level of random noise $\langle \epsilon(x,0) \rangle \sim 10^{-3}$. The seeding was reduced linearly to zero at $t = 10\tau_g$. The steady-state results shown in the figures were obtained by integrating for several hundred characteristic time constants.

Consider first the response of a self-imaging resonator, containing only a gain medium, to partially correlated input signals. The correlation of the resonator fields $h_{12}^{(g)}$ as a function of the input signal correlation $h_{12}^{(0)}$ is shown in Fig. 6(a) for three different values of the coupling constant. The correlation of the resonator fields increases as the input field correlation is increased. The oscillating intensity also increases monotonically with the spatial correlation of the input signals, as is shown in Fig. 6(b). When the signals have the same spatial mode the value of the coupling coefficient is Γ_g. When the signals are spatially uncorrelated the effective value of the coupling coefficient is reduced to $\Gamma_g/2$. In between, the coupling coefficient and the oscillating intensity increase as the spatial correlation is increased. It is also apparent that the fields inside the resonator are more strongly correlated than the input signals. The tendency of the resonator to increase the spatial correlation decreases as the nonlinear coupling is increased. For $\Gamma_g l_g = 18$ there is only a small difference between the correlation of the input and resonator signals. Nonetheless, the resonator with gain only does not lead to a useful spatial mapping of the input signals. The intensity distributions of the oscillating signals are strongly overlapped in the gain medium, and cannot be separated. Taking the spatial Fourier transform of the oscillating signals leads to distributions that are spread out over the available transverse aperture of the resonator. The signals are not localized in the Fourier transform plane.

In order to obtain oscillating signals that are well localized spatially a loss crystal is added to the resonator. The resulting correlations at the output of the gain and loss media are shown in Fig. 7. Introducing the loss medium leads to an even greater increase in the spatial correlation of the resonator fields than is observed in the resonator with gain only. Because the loss saturation is maximized in regions where the resonator fields have high intensity, the loss medium tends to 'pull' the resonator modes together. This results in

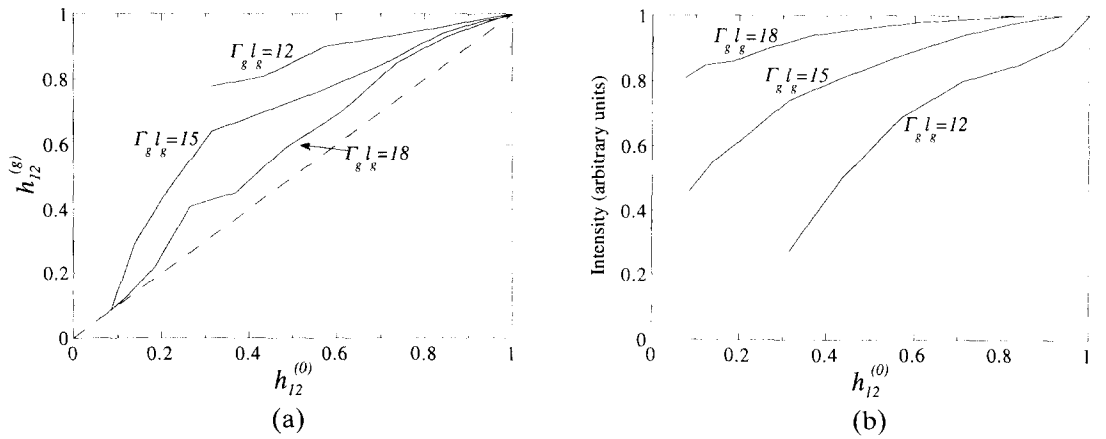

Fig. 6. Spatial correlation (a) and intensity (b) of the fields in a self-imaging resonator with gain only.

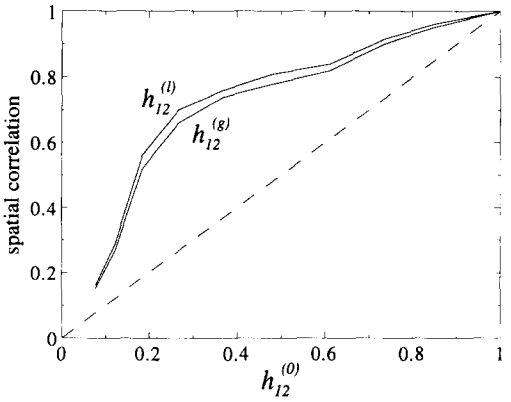

Fig. 7. Spatial correlation of the resonator fields in a self-imaging resonator with gain and loss. The coupling coefficients were $\Gamma_g l_g = 15$ and $\Gamma_l l_l = -2$.

$h_{12}^{(l)} > h_{12}^{(g)}$. Each of the input signals now maps onto a localized intensity distribution in the plane of the loss medium, as shown in Fig. 8. Note that the intensity profiles shown in Fig. 8 are well localized but, because of their mutual interaction, they do not have the smooth Gaussian-like shape that is obtained when the resonator is pumped by a single input signal. The calculated profiles correspond to solutions that maximize the net round-trip gain (amplification–loss). When the resonator is pumped by several signals the result is localized modes that have a complicated transverse variation of both intensity and phase. The Fourier transform of the gain pump profile given by equations (4) gives a spot in the loss medium with diameter $2\omega_l = 18$ μm. The region covered by the two calculated spots in Fig. 8(b) is about 35 μm, or twice as wide. The transverse phase variations, not shown in the figure, also contribute to the calculated value of the correlation. Observations of the intensity alone tend to make the correlation appear higher than it actually is. This is also evident in the experimental data of Fig. 4.

In order to demonstrate clearly the topology-preserving nature of the resonator we consider the case of three partially correlated input signals. The input and resonator correlations are shown in Fig. 9. The ordering of the resonator correlations agrees with the ordering of the input correlations. Thus the topology of the inputs, as measured by their spatial correlation, is preserved.

5. PLANE WAVE ANALYSIS

In this section we consider a simplified, but analytically tractable, model in order to gain insight into the reason for the observed behavior. Different input signals are mapped onto different resonator modes because this maximizes the energy transfer to the resonator. We know on the basis of a linear stability analysis of a multimode ring resonator with gain only (unpublished), that orthogonal signals always prefer to map to orthogonal resonator modes. In the resonator with gain and loss the situation may in principle be different. If the input signals mapped onto the same resonator modes, then the gain would be lower. However, the loss would also be lower. In order for separate resonator modes to be the preferred state, the net energy transfer (gain–loss), must be maximized. Otherwise the feature extractor, and the topology-preserving map, would not work.

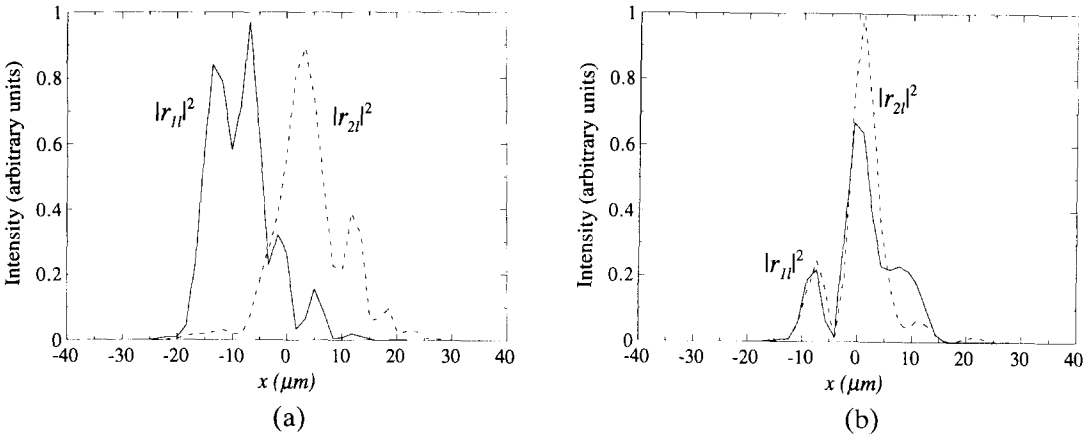

Fig. 8. Intensity profile of the localized modes at the output of the loss medium for (a) $h_{12}^{(0)} = 2 \times 10^{-9}$ giving $h_{12}^{(l)} = 1.2 \times 10^{-4}$ and (b) $h_{12}^{(0)} = 0.17$ giving $h_{12}^{(l)} = 0.52$. The origin of the x-coordinate has been chosen for convenience, and does not correspond to the axis of the resonator.

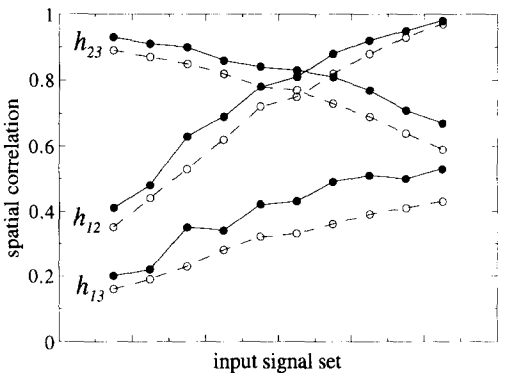

Fig. 9. Spatial correlations of the resonator fields at the output of the loss medium when the resonator is pumped by three input signals. The dashed lines are input signal correlations and the solid lines are resonator correlations at the output of the loss medium. The coupling coefficients were $\Gamma_g l_g = 20$ and $\Gamma_l l_l = -3$.

Equations (1) and (2) are not easily solved analytically. We will therefore study them in a steady-state plane-wave limit [18]. The equations of motion are then

$$\frac{\mathrm{d}r_{ij,m}}{\mathrm{d}z} = \sum_{i'} g_{ii',m} s_{i'j,m}, \tag{6a}$$

$$\frac{\mathrm{d}s_{ij,m}}{\mathrm{d}z} = -\sum_{i'} g^*_{i'i,m} r_{i'j,m}, \tag{6b}$$

$$g_{ii',m} = \frac{\Gamma_m}{2I_m} \sum_j r_{ij,m} s^*_{i'j,m}. \tag{6c}$$

$s_{ij,m}$, $r_{ij,m}$ are signal and resonator fields with spatial mode i and temporal mode j, and $m = \{g, l\}$ labels the gain or loss medium. Note that in contrast to equations (1) and (2), Bragg-matching has been implicitly assumed. Thus $r_{ij,m}$, the resonator field with spatial mode i only scatters off the grating due to the interference of $r_{ij,m}$ with $s_{i'j,m}$. Resonator

fields in different spatial modes do not interact directly with each other through shared gratings. This formulation of the equations of motion corresponds to the feature extractor experiment.

Equations (6) are to be applied to the idealized resonator models shown in Fig. 10. Consider the situation shown in Fig. 10(a) where the input signals map to spatially orthogonal resonator modes. In this case, different temporal modes write Bragg-mismatched gratings and equations (6) decouple. The solution for the change in intensity of a resonator beam due to a gain or loss interaction is

$$\frac{I_r(\text{out})}{I_r(\text{in})} = \frac{1 + M}{1 + Me^{-X/N}}, \tag{7}$$

where $M = I_s(\text{in})/I_r(\text{in})$, $X = \pm\Gamma l$ for gain or loss, respectively, Γ_m is assured real, N is the number of input signals and, for simplicity, we have assumed equal intensities in each temporal mode. The resonator intensity in one temporal mode at the input to the gain medium is found by applying equation (7) for the gain and loss media, multiplying by the cavity reflectivity, and requiring the round-trip gain to be unity in steady state. This results in a cubic equation for $\eta = I_{r,g}(0)/I_{s,g}(0)$. Using $\eta \ll 1$, which is valid for low cavity reflectivity, gives the following quadratic equation for η:

$$[1 + M_{gl}\exp(\Gamma_l l_l/N)]\eta^2 + [\exp(-\Gamma_g l_g/N) + 2M_{gl}\exp\{((\Gamma_l l_l - \Gamma_g l_g)/N)\} - (1 + M_{gl})\exp(-C)]\eta + M_{gl}\exp(-\Gamma_g/N)[\exp(\Gamma_l l_l - \Gamma_g l_g)/N) - \exp(-C)] = 0. \tag{8}$$

Here $M_{gl} = I_{sl}(0)/I_{sg}(0)$. Putting $M_{gl} = 0$ we recover the well-known expression for the oscillating intensity in a photorefractive ring resonator with gain only [21]. The ring resonator with saturable gain and loss may be bistable [22, 23]. The two roots of equation

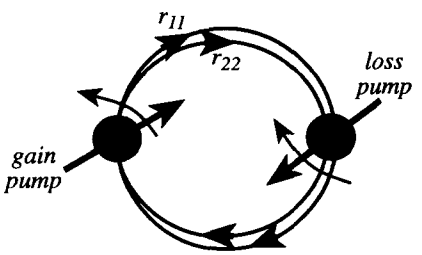

(a)

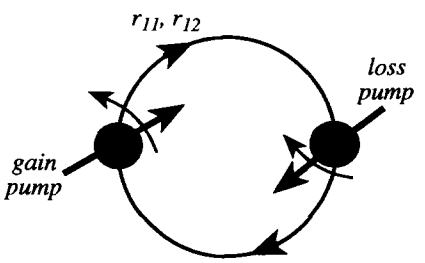

(b)

Fig. 10. Plane wave models of the self-imaging resonator for two input signals. In (a) the input signals map onto spatially orthogonal resonator modes, in (b) the input signals map onto the same resonator mode.

(8) correspond to the upper and lower branches of the bistability curve. We will assume that the resonator is strongly seeded so that the observed value of η lies on the upper branch. η is plotted for different values of the gain and loss in Fig. 11.

We now wish to compare the value of η obtained when all signals map onto the same resonator mode. Equations (6) must be solved for N resonator fields, $r_{11,m} \cdots r_{1N,m}$ interacting with N^2 signal fields. Analytic solutions may be found by assuming symmetric interactions ($r_{11,m} = \ldots = r_{1N,m}$, $s_{11,m} = \ldots = s_{NN,m}$, and all $s_{ij,m}$ equal for $i \neq j$). The equations of motion then reduce to

$$\frac{dr_{11,m}}{dz} = g_m[s_{11,m} + (N-1)s_{12,m}], \tag{9a}$$

$$\frac{ds_{11,m}}{dz} = \frac{ds_{12,m}}{dz} = -g_m^* r_{11,m}, \tag{9b}$$

$$g_m = \frac{\Gamma_m}{2I_m} r_{11,m}[s_{11,m}^* + (N-1)s_{12,m}^*]. \tag{9c}$$

Solving for the change in the resonator intensity using $s_{ij,m}(0) = 0$, for $i \neq j$ gives

$$\frac{I_r(\text{out})}{I_r(\text{in})} = \frac{1 + M/N}{1 + (M/N)\exp[-\{1 + (M/N)\}X/(1+M)]}, \tag{10}$$

where $X = \pm \Gamma l$ for gain or loss, respectively. Using $M_g \gg N$ and $M_l \ll 1$ gives the following quadratic equation for η:

$$N^2[1 + M_{gl}\exp(\Gamma_l l_l)]\eta^2 + N[\exp(-\Gamma_g l_g/N) + 2M_{gl}\exp(\Gamma_l l_l - \Gamma_g l_g/N) - (1 + M_{gl})\exp(-C)]\eta + M_{gl}\exp(-\Gamma_g/N)[\exp(\Gamma_l l_l - \Gamma_g l_g/N) - \exp(-C)] = 0. \tag{11}$$

Referring to Fig. 11 we see that the oscillating intensity is always highest when the signals map to orthogonal spatial modes. Even though the loss crystal serves to attract the signals into the same spatial mode, the effect of the gain crystal, which repels the signals, is always stronger. The same qualitative behavior should also apply to topology-preserving mappings of correlated signals.

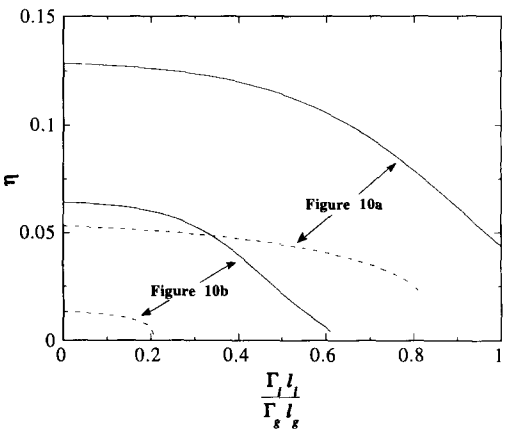

Fig. 11. Oscillating intensity as found from equations (8) and (11). The solid lines are for $N = 2$ and the broken lines are for $N = 4$. The parameters were: $\Gamma_g l_g = 10$, $C = 2$, and $M_{gl} = 0.01$.

6. DISCUSSION

We have demonstrated a photorefractive resonator that embodies the functionality of a computational algorithm in the dynamics of a physical system. The resonator supports a continuous family of spatially localized transverse modes. When the resonator is pumped by an information bearing beam the transverse modes self-organize to generate a mapping of input signals onto localized resonator modes. The mapping is topology-preserving. Similar input signals, as measured by their inner product, are mapped onto similar resonator modes. Because the photorefractive gain is mediated by a volume hologram, the measure of similarity is an inner product. Different physical gain mechanisms could, in principle, be sensitive to different measures of similarity.

In the geometry studied here, the mapping is from a one-dimensional input space to a one-dimensional output space. Numerical simulations of the equations of motion show that the mapping is compressed. The spatial overlap of the resonator fields is proportional to the spatial overlap of the input fields raised to a power less than one. Futhermore, the intensity distributions of the localized modes depart from a smooth Gaussian-like shape when the modes are partially correlated. In this situation, observations of the intensity distribution alone, make the resonator modes appear more highly correlated than they actually are.

Acknowledgement—This work was supported by NSF grant PHY90-12244. M.S. thanks the Air Force Office of Scientific Research for a laboratory graduate fellowship.

REFERENCES

1. D. Z. Anderson, Coherent optical eigenstate memory, *Opt. Lett.* **11**, 56–58 (1986).
2. D. Z. Anderson and M. C. Erie, Resonator memories and optical novelty filters, *Opt. Engng.* **26**, 434–444 (1987).
3. A. Yariv and S.-K. Kwong, Associative memories based on message-bearing optical modes in phase-conjugate resonators, *Opt. Lett.* **11**, 186–188 (1986).
4. B. H. Soffer, G. J. Dunning, Y. Owechko and E. Marom, Associative holographic memory with feedback using phase-conjugate mirrors, *Opt. Lett.* **11**, 118–120 (1986).
5. M. Brambilla, L. A. Lugiato, M. V. Pinna, F. Prati, P. Pagani, P. Vanotti, M. Y. Li and C. O. Weiss, The laser as nonlinear element for an optical associative memory, *Opt. Commun.* **92**, 145–164 (1992).
6. M. Saffman, C. Benkert and D. Z. Anderson, Self-organizing photorefractive frequency demultiplexer, *Opt. Lett.* **16**, 1993–1995 (1991).
7. D. Z. Anderson, C. Benkert, V. Hebler, J.-S. Jang, D. Montgomery and M. Saffman, Optical implementation of a self-organizing feature extractor, in *Advances in Neural-Information Processing Systems IV*, edited by J. E. Moody, S. J. Hanson, and R. P. Lippmann, pp. 821–828. Morgan Kaufmann, San Mateo, CA (1992).
8. M. Saffman, D. Montgomery and D. Z. Anderson, Collapse of a transverse mode continuum in a self-imaging photorefractively pumped ring resonator, *Opt. Lett.* **19**, 518–520 (1994).
9. T. Kohonen, *Self-organization and Associative Memory*, 3rd Edn. Springer, Berlin (1989).
10. H. Ritter, T. Martinetz and K. Schulten, *Neural Computation and Self-organizing Maps*, Addison-Wesley, Reading, MA (1992).
11. K. Obermayer, G. G. Blasdel and K. Schulten, Statistical-mechanical analysis of self-organization and pattern formation during the development of visual maps, *Phys. Rev.* **A45**, 7568–7589 (1992).
12. T. Kohenen, Self-organized formation of topologically correct feature maps, *Biol. Cybernetics* **43**, 59–69 (1982).
13. C. Benkert and D. Z. Anderson, Controlled competitive dynamics in a photorefractive ring oscillator: Winner-takes-all and the voting paradox dynamics, *Phys. Rev.* **A44**, 4633–4638 (1991).
14. B. Fischer, O. Werner, M. Horowitz and A. Lewis, Passive transverse-mode organization in a photorefractive oscillator with saturable absorber, *Appl. Phys. Lett.* **58**, 2729–2731 (1991).
15. V. Yu. Bazhenov, V. B. Taranenko and M. V. Vasnetsov, WTA-dynamics in large aperture active cavity with saturable absorber, *Proc. Soc. Photo-Opt. Instrum. Eng.* **1806**, 14–21 (1993).
16. M. Saffman, D. Montgomery, A. A. Zozulya and D. Z. Anderson, Wandering excitations in a photorefractive ring resonator, in *Photorefractive Materials, Effects, and Devices Technical Digest* paper ThD11.3. Optical Society of America, Washington, DC (1993).

17. G. D'Alessandro, Spatiotemporal dynamics of a unidirectional ring oscillator with photorefractive gain, *Phys. Rev.* **A46**, 2791–2802 (1992).
18. D. Z. Anderson, M. Saffman and A. Hermanns, Manipulating the information carried by an optical beam with reflexive photorefractive beam coupling, *J. Opt. Soc. Am.* **B**, to appear.
19. M. Saffman and D. Z. Anderson, Mode multiplexing and holographic demultiplexing communication channels on a multimode fiber, *Opt. Lett.* **16**, 300–302 (1991).
20. W. H. Press, S. A. Teukolsky, W. T. Vetterling and B. P. Flannery, *Numerical Recipes in FORTRAN. The Art of Scientific Computing*, 2nd Edn. Cambridge University Press, Cambridge (1992).
21. J. O. White, M. Cronin-Golomb, B. Fischer and A. Yariv, Coherent oscillation by self-induced gratings in the photorefractive crystal $BaTiO_3$, *Appl. Phys. Lett.* **40**, 450–452 (1982).
22. D. M. Lininger, P. J. Martin and D. Z. Anderson, Bistable ring resonator utilizing saturable photorefractive gain and loss, *Opt. Lett.* **14**, 697–699 (1989).
23. D. M. Lininger, D. D. Crouch, P. J. Martin and D. Z. Anderson, Theory of bistability and self-pulsing in a ring resonator with saturable photorefractive gain and loss, *Opt. Commun.* **76**, 89–96 (1990).